Location-dependent Raman transition in gravity-gradient measurements using dual atom interferometers

Yuping Wang,[1,2,3] Jiaqi Zhong,[1,4,*] Hongwei Song,[1,5] Lei Zhu,[1,3] Yimin Li,[1,3] Xi Chen,[1,4] Runbing Li,[1,4] Jin Wang,[1,4,†] and Mingsheng Zhan[1,4]

[1]*State Key Laboratory of Magnetic Resonance and Atomic and Molecular Physics, Wuhan Institute of Physics and Mathematics, Chinese Academy of Sciences, Wuhan 430071, China*

[2]*School of Electronic Information and Electronic Engineering, Tianshui Normal University, Tianshui 741000, China*

[3]*University of Chinese Academy of Sciences, Beijing 100049, China*

[4]*Center for Cold Atom Physics, Chinese Academy of Sciences, Wuhan 430071, China*

[5]*School of Optical and Electronic Information, Huazhong University of Science and Technology, Wuhan 430074, China*

(Received 5 March 2017; published 11 May 2017)

The location-dependent Raman transition was investigated based on dual atom interferometers which were designed for gravity-gradient measurements. The cross talk between the Raman beam pairs generated by an electro-optical modulator make the Raman transition location dependent. Therefore, the fringe contrast also depends on the location where the Raman pulses interact with the atoms, so it is important to adjust the interaction location to optimize the precision of the gravity-gradient measurements. To further reduce the residual cross talk, the detuning of the Raman beams for ^{85}Rb atoms was controlled using the saturated absorption spectra of the ^{87}Rb atoms. The optimal location for the Raman transition was determined by theoretical analysis and modulation experiments, and the atomic trajectory was optimized and applied to the gravity-gradient measurements. The resolution of the differential gravity measurement evaluated by the Allan deviation was 4.9×10^{-9} m/s^2 @ 15 000 s, and the corresponding resolution of the gravity gradient measurement was 7.4 E @ 15 000 s.

DOI: 10.1103/PhysRevA.95.053612

I. INTRODUCTION

Atom interferometers (AIs) have been applied in precision measurements, such as the testing of the weak equivalence principle [1], measurement of rotation [2,3], and measurement of gravity [4,5]. However, the vibrational noise present in atom interferometry limits its sensitivity in these measurements. Fortunately, the atom gravity gradiometers (AGGs) based on dual AIs [6] and single AIs [7,8] have been demonstrated to eliminate the influence of the common-mode vibrational noise, and the sensitivities have been improved by several orders of magnitude. Further, AGGs have been applied as powerful tools in the determination of the gravitational constant [9–11] and measurement of the Earth's gravity gradient [12]. A compact movable AGG for navigation, geodesy, underground structure detection, and mineral exploration was demonstrated in 2009 [13]. Also, an AGG for mapping the global gravity field from space is still ongoing [14]. In gravity-gradient measurements with dual AIs, the Raman beam pairs interact simultaneously with atom clouds at different locations. The Raman transition is very important for the performance of an AGG, and a Raman beam pair for Raman transition is usually produced by employing either optical phase-locking loops [15,16], acousto-optic modulators (AOMs), or electro-optic modulators (EOMs). The EOM method is popularly used to produce low-noise, high-intensity, stable Raman beams [17–19] for a compact AI. However, multiple Raman beam pairs consisting of the carrier and sidebands [20–22] are present in the EOM method, and each pair of Raman beams drives a Raman transition. Consequently, the cross talk of the multiple Raman beam pairs cause the effective Rabi frequency to be location dependent in atom interferometry [20,21]; thus the fringe contrast also depends on the location where the Raman pulses interact with the atoms. To optimize the precision of the gravity-gradient measurement, it is important to investigate the location-dependent Raman transition that exists in dual AIs.

In this paper, we study the location-dependent Raman transition in AIs, and investigate its effect on the gravity-gradient measurement. Unlike the gravity gradiometer that adopts two AIs with separated vacuum chambers [12,14], our compact gravity gradiometer is composed of two identical ^{85}Rb AIs that share the same vacuum chamber. This configuration is useful for eliminating the wave-front distortion and the steering noise [23] of the Raman beams caused by windows and air flux. To reduce the residual cross talk, we control the detuning of the Raman beams for ^{85}Rb atoms using the saturated absorption spectra of ^{87}Rb atoms, which also improved the stability and reliability of the Raman beams. Based on theoretical analysis and modulation experiments, the flight trajectory of the atoms was carefully designed, the Raman transition was optimized, measurement of the gravity gradient was demonstrated, and the results were evaluated.

II. LOCATION-DEPENDENT RAMAN TRANSITION IN THE GRAVITY-GRADIENT MEASUREMENT

First we consider the dual ^{85}Rb AI used for measuring the vertical component of the gravity-gradient tensor. The vertical separation between the two AIs was L. The Raman beam pairs were generated by a phase-modulation method wherein two ^{85}Rb atom clouds were prepared in the individual AIs and were launched vertically. Next, a sequence of stimulated Raman transitions were applied to the atom clouds to split, redirect,

*jqzhong@wipm.ac.cn
†wangjin@wipm.ac.cn

and recombine the atomic wave packets, and thereby to form two interference loops. The gravity-gradient information was extracted by measuring the phase difference existing between the interference fringes of the two interference loops. The Raman transition plays an important role in the gravity-gradient measurement. Typically, the Raman transition in atom interferometry is independent of location where Raman beams interact with atoms if the Raman beams are ideal. For Raman beams generated by a phase modulation, the performance of the Raman transition depends on the location, and this location-dependent Raman transition influences the accuracy of the gravity-gradient measurement.

To analyze the dependence of the Raman transition on location, we consider an atom with three states: a lower ground state $|g\rangle$ (for ^{85}Rb, $|F=2,m_F=0\rangle$), an upper ground state $|e\rangle$ (for ^{85}Rb, $|F=3,m_F=0\rangle$) and an excited state $|i\rangle$. The frequency separation between the ground states $|e\rangle$ and $|g\rangle$ is ω_{eg}. The Raman beams are generated by an EOM and then retroreflected by a mirror, where the frequency of the EOMs driving the microwave is ω_m (where $\omega_m \approx \omega_{eg}$), and the distance between the atoms and the mirror is l. In the weak phase-modulation limit, suppose two pairs of Raman beams exist that consist of the carrier with the frequency ω_c and the ±1 order sidebands with the frequency $\omega_{\pm1}$. One Raman pair consists of a carrier (ω_c, propagating upward) and the +1-order sideband ($\omega_{+1}=\omega_c+\omega_m$, propagating downward), where the single-photon detuning of the Raman transition is Δ_{+1} (according to the excited state $|i\rangle$). The other Raman pair consists of the carrier (ω_c, propagating downward) and the -1-order sideband ($\omega_c-\omega_m$, propagating upward), where the single-photon detuning is Δ_{-1} ($\Delta_{-1}=\Delta_{+1}+\omega_m$). The electric field that drives the resonant two-photon transition between the ground states $|g\rangle$ and $|e\rangle$ is written as

$$\begin{aligned} E = {} & E_{+1}\cos(\omega_{+1}t-k_{+1}z+\varphi_0)+E_c\cos(\omega_c t+k_c z+\phi_c) \\ & +E_c\cos(\omega_c t-k_c z+\varphi_0) \\ & +E_{-1}\cos(\omega_{-1}t+k_{-1}z+\phi_{-1}), \end{aligned} \tag{1}$$

where $k_j=\omega_j/c$ is the wave vector, φ_0 is the initial phase of the incident Raman beams, $\phi_j=-2k_jl+\varphi_0$ is the phase of the retroreflected Raman beams, and $-2k_jl$ is the delayed phase introduced by an additional distance $2l$.

The atom interacts with the two Raman beam pairs, and each Raman beam pair drives a two-photon Raman transition between the two ground states $|g\rangle$ and $|e\rangle$ via the intermediate state $|i\rangle$. Consequently, the cross talk between different Raman beam pairs causes the Raman transition to be location dependent. Both Raman pairs are resonant with the hyperfine transition of atoms, and the effective Rabi frequency is the combination of the individual Rabi frequencies. Considering the phase of each Rabi frequency [24], the effective Rabi frequency can be written as

$$\Omega(l)_{\text{eff}}=\frac{\Omega_{+1}^{*}\Omega_c}{2\Delta_{+1}}e^{i2k_cl}+\frac{\Omega_c^{*}\Omega_{-1}}{2\Delta_{-1}}e^{i2k_{-1}l}, \tag{2}$$

where the first term on the right-hand side $2k_jl=\varphi_0-\phi_j$ is the Rabi frequency of the Raman beam pair ω_c and ω_{+1}, and the second term is the Rabi frequency of the Raman beam pair ω_c and ω_{-1}. Taking into account the symmetry of the sideband, $\Omega_{+1}^{*}\Omega_c=\Omega_c^{*}\Omega_{-1}$, the square of the effective Rabi frequency can be written as

$$\Omega(l)_{\text{eff}}^2=\Omega_0^2\left[1+\left(\frac{\Delta_{+1}}{\Delta_{-1}}\right)^2+2\frac{\Delta_{+1}}{\Delta_{-1}}\cos\left(\frac{2\pi l}{\lambda_m/2}\right)\right], \tag{3}$$

where $\Omega_0=\frac{\Omega_{+1}^{*}\Omega_c}{2\Delta_{+1}}$ is the Rabi frequency of the Raman beam pair (ω_c and $\omega_c+\omega_m$) and $\lambda_m=2\pi/(k_c-k_{-1})$ is the wavelength of the microwave. Obviously, $\Omega(l)_{\text{eff}}$ is a periodic function of $\lambda_m/2$, and its amplitude depends on Δ_{+1}. When a Raman pulse with a duration of τ is applied to atoms in the initial state $|g\rangle$, the probability of atoms being in the state $|e\rangle$ is given as

$$P_e(l)=\frac{\Omega(l)_{\text{eff}}^2}{\Omega(l)_{\text{eff}}^2+\delta^2}\sin^2\left(\sqrt{\Omega(l)_{\text{eff}}^2+\delta^2}\frac{\tau}{2}\right), \tag{4}$$

where δ is the difference between the two-photon detuning and the relative ac Stark shift of the two levels. Compared to $\Omega(l)_{\text{eff}}$, δ is negligible. Therefore, ignoring δ in Eq. (4), the probability of atoms being in state $|e\rangle$ is simplified as

$$P_e(l)=\tfrac{1}{2}[1-\cos(|\Omega(l)_{\text{eff}}|\tau)]. \tag{5}$$

Obviously, when the duration τ is a constant, $P_e(l)$ also has a spatial periodicity of $\lambda_m/2$. For ^{85}Rb atoms, $\lambda_m/2$ is 5 cm.

In dual AIs using two Raman beam pairs, the gravity gradient is measured using two atom clouds separated by L. When two atom clouds interact with Raman beam pairs, the distances from atom cloud 2 (AC2) and atom cloud 1 (AC1) to the mirror are l and $l+L$, respectively. Then, the effective Rabi frequency of AC2 is the same as that given in Eq. (3), and the probability of AC2 is the same as that given in Eq. (5). Therefore, substituting $l+L$ for l and taking $L=n\lambda_m/2+\Delta l$ into Eqs. (3) and (5), the effective Rabi frequency of AC1 can be written as

$$|\Omega(l+L)_{\text{eff}}|=|\Omega(l+\Delta l)_{\text{eff}}|, \tag{6}$$

and the probability of AC1 can be written as

$$P_e(l+L)=P_e(l+\Delta l), \tag{7}$$

where n is an integer and $0\leqslant\Delta l<\lambda_m/2$. According to Eqs. (6) and (7), if the separation between two atom clouds, L, is an integer multiple of the spatial wavelength $\lambda_m/2$ ($\Delta l=0$), the effective Rabi frequency of AC1 is obtained by shifting that of AC2 by an integer multiple of the spatial wavelength $\lambda_m/2$; that is, $|\Omega(l+L)_{\text{eff}}|=|\Omega(l)_{\text{eff}}|$. Similarly, the probability of AC1 is $P_e(l+L)=P_e(l)$. This means a Raman pulse synchronously interacts with two atom clouds at different locations, and a π pulse (or $\pi/2$ pulse) for one atom cloud is also a π pulse (or $\pi/2$ pulse) for the other atom cloud. If L is not an integer multiple of $\lambda_m/2$ ($0<\Delta l<\lambda_m/2$), however, the effective Rabi frequency and the probability of AC1 have a delayed phase, $2k_m\Delta l$, with respect to those of AC2 for an arbitrary location l, where $k_m=2\pi/\lambda_m$ is

the microwave wave vector. This means that a Raman pulse cannot synchronously operate on two atom clouds at different locations, and a π pulse (or $\pi/2$ pulse) for one atom cloud will definitely not be a π pulse (or $\pi/2$ pulse) for the other atom cloud. When a Raman π pulse interacts with two atom clouds, there is a big difference (even up to 30%) between the probabilities of AC2 and AC1 in $|e\rangle$.

Considering the discussion above, the location-dependent Raman transition affects the fringe contrast of both AIs, and the separation between the two AIs determines if their fringe contrasts are simultaneously optimized. To improve the accuracy of the gravity-gradient measurement, the separation between two atom clouds, L, should be designed as an integer multiple of $\lambda_m/2$. Unfortunately, in an actual AGG, L is not an exact integer multiple of $\lambda_m/2$. According to Eqs. (3)–(7), one can optimize the location-dependent Raman transition in the gravity-gradient measurement using dual differential AIs.

III. EXPERIMENTAL SETUP

The atom gravity gradiometer consisted of a dual AI with vertical configuration; its schematic diagram is shown in Fig. 1. Two AIs shared an ultrahigh-vacuum chamber (pressure $< 10^{-8}$ Pa). The Raman beams were delivered by polarization-maintaining optical fibers that traveled from the laser module to the top window of the vacuum chamber, and were then retroreflected by a mirror mounted under the bottom window. The Raman beams were expanded into collimated beams with a $1/e^2$ diameter of 2 cm and a power of 100 mW. To maintain the orthogonal polarization of incident and retroreflected Raman beams, a quarter-wave plate was inserted between the mirror and the bottom window. Because the Raman beams and the mirror were shared in this configuration, it was immune to common phase noise. Each AI

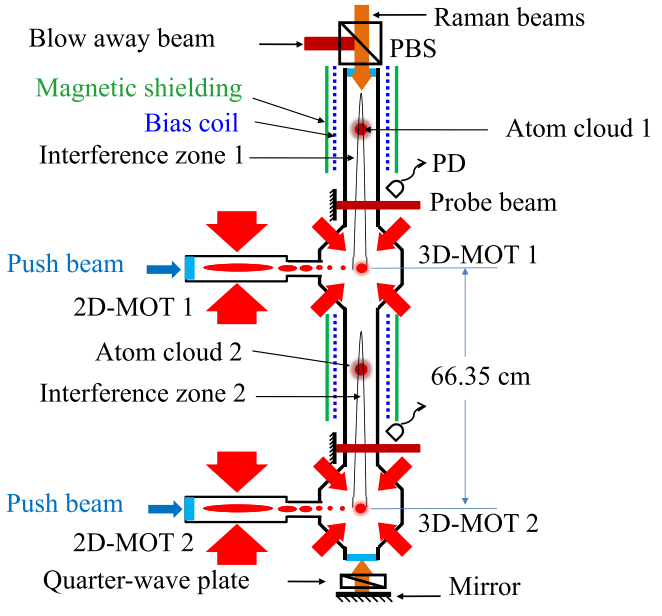

FIG. 1. The schematic diagram of the atom gravity gradiometer. PBS: polarizing beam splitter; PD: photo detector; 2D-MOT: two-dimensional magneto-optical trap; 3D-MOT: three-dimensional magneto-optical trap.

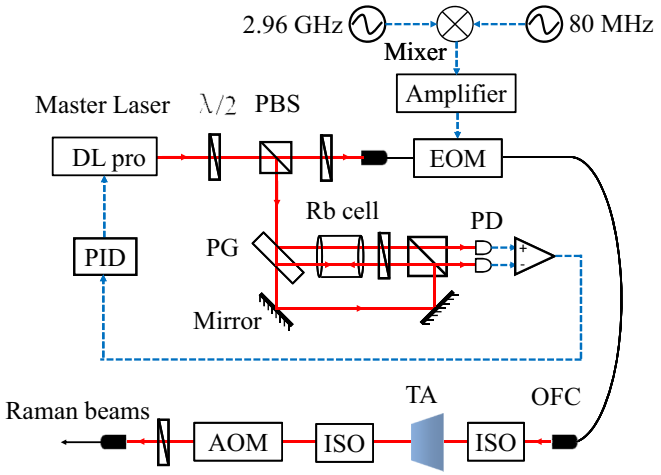

FIG. 2. The schematic diagram of Raman beams. PD: photodetector; PBS: polarized beam splitter; PG: plate glass; OFC: optical fiber coupler.

comprised a two-dimensional magneto-optical trap (2D-MOT) [25], a three-dimensional magneto-optical trap (3D-MOT), an interference zone, and a detecting zone. The 2D-MOT provided a radially cooled ^{85}Rb beam for the 3D-MOT, and a push beam was applied to enhance the atomic flux so that the 3D-MOT could trap more than 1×10^8 atoms within 1 s while maintaining an ultrahigh vacuum. Precooled ^{85}Rb atoms in the 2D-MOT were pushed to and trapped in the center of the 3D-MOT within 1 s, and then were further cooled to 5 μK and launched vertically by a moving optical molasses. Atom clouds trapped in both MOTs were launched to interference zones simultaneously, and a Raman pulse sequence was applied to achieve atom interferometry. A bias magnetic field of 200 mG was applied to define the quantization axis, where the stray magnetic fields around the interference zones were shielded by a factor of 50 using μ-metal films. The detecting zones were set at 11 cm above the 3D-MOTs, and the separation between the two 3D-MOTs was 66.35 cm.

A schematic diagram of the Raman beams is shown in Fig. 2. The Raman beams were taken from the output of a master laser (Toptica, DL Pro), whose linewidth was 200 kHz and output power was 60 mW. To obtain a large detuning (1.3 GHz) of the Raman beams for ^{85}Rb, we locked the master laser to the cross peak ($5S_{1/2}, F = 2$ to $5P_{3/2}, F' = 1,3$ transitions) of the ^{87}Rb atoms via saturated absorption spectroscopy, and generated Raman beams with a frequency difference of 3.04 GHz by a fiber EOM (Eospace, PM-0K5-10-PFU-PFA-780) [21]. The Raman beams were amplified by a homemade tapered amplifier (TA), and their frequencies were slightly adjusted by an 80-MHz AOM with a double-pass configuration. The 3.04 GHz driving signal for the fiber EOM was generated by mixing a 2.96-GHz microwave signal and an 80-MHz radio signal, where the microwave signal was generated by a signal generator (Rigol, DSG3060) and the radio signal was supplied by an arbitrary waveform generator (Agilent, 33250A). A microwave amplifier (Mini-Circuits ZVE-8GX+) was used to amplify the 3.04 GHz signal. Finally, the radio source was chirped to compensate for the gravity-induced Doppler shift.

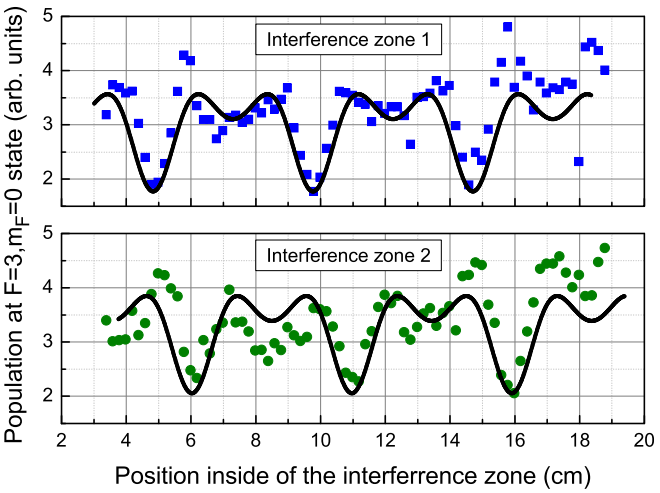

FIG. 3. Population of the $F = 3$, $m_F = 0$ state after applying the Raman pulse with duration of 20 μs along interference zone 1 (blue squares) and interference zone 2 (green dots). The position is referenced to the bottom of the individual interference zone.

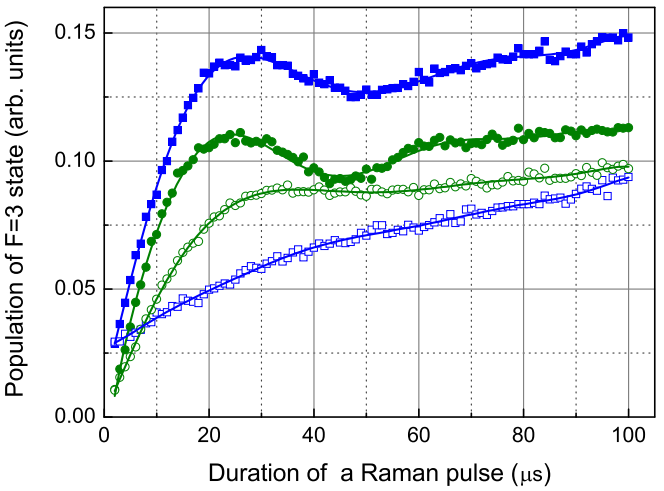

FIG. 4. Comparison of Rabi oscillations of atoms at two locations. The blue squares and blue boxes are Rabi oscillations at $z_1 = 7.78$ cm and $z_2 = 14.78$ cm in interference zone 1, respectively. The green dots and green circles are Rabi oscillations at z_1 and z_2 in interference zone 2, respectively. The solid curves are the fits to the individual data.

IV. OPTIMIZATION OF LOCATION-DEPENDENT RAMAN TRANSITION IN A DUAL ATOM INTERFEROMETER

We experimentally investigate the location-dependent Raman transition by monitoring the population of $F = 3, m_F = 0$ versus the interaction position. First, the atom clouds are launched to the top of the interference zones, whereupon a Raman pulse is applied to interact with the free-fall atom clouds. The differential frequency of the Raman pulse is scanned with a step of 10 kHz, and the resonance signal of the transition from $F = 2$, $m_F = 0$ to $F = 3$, $m_F = 0$ is obtained. Figure 3 plots the populations of the $F = 3$, $m_F = 0$ state after applying the Raman pulse with a duration of 20 μs to interference zone 1 (IZ1) (blue squares in Fig. 3) and interference zone 2 (IZ2) (green dots in Fig. 3), and also plotted are the fits based on Eq. (4) (black lines in Fig. 3; $\omega_m = 2\pi \times 3.035$ GHz, $\Delta_{+1} = 2\pi \times 1.312$ GHz, $\Delta_{-1} = 2\pi \times 4.347$ GHz, $\tau = 20$ μs). The fitted parameters δ and Ω_0 are 0.04 Hz and $2\pi \times 22.6$ kHz, respectively. According to the population in Fig. 3, there are three minima spaced by 5 cm, as expected, while the theoretical fits indicate that the population varies simultaneously with a spatial period of $\lambda_m/2$. The baseline of the gravity gradiometer used is 66.35 cm, which is not an integer multiple of 5 cm. This causes the population of IZ1 to be shifted by 1.23 cm according to that of IZ2. This roughly agrees with the theoretical value of 1.35 cm.

The Rabi oscillation also varies with the interaction location. We select two typical positions inside the interference zones, $z_1 = 7.78$ cm and $z_2 = 14.78$ cm, where according to Fig. 3, z_1 (z_2) corresponds to the location where the population is near its maximum (minimum) for IZ1. The experimental results are shown in Fig. 4. For IZ1, the population of the $F = 3$ state at z_1 (blue squares in Fig. 4) is a damped oscillation with a frequency of 20 kHz, while that at z_2 (blue boxes in Fig. 4) slowly increases with the duration of the Raman pulse. These results imply that the efficiency of the Raman transition at z_1 is high, while it is at its lowest at z_2; i.e., a Raman π pulse can coherently transfer atoms between two hyperfine ground states at z_1 but not at z_2. For IZ2, the population of the $F = 3$ state at z_1 (green dots in Fig. 4) is a damped oscillation with a frequency of 22 kHz, while that at z_2 (green circles in Fig. 4) is a critically damped oscillation. Therefore, the coherence of the atoms at z_1 is better than that at z_2, and a Raman π pulse can coherently transfer atoms between the two hyperfine ground states at both z_1 and z_2. Consequently, the positions where each Raman pulse interacts with atoms can be used to optimize the Raman transition. Substituting Δ_{+1}, Δ_{-1}, Ω_0, and ω_m into Eq. (3), we find that $\Omega_{\text{eff}}(l)$ reaches a minimum (16 kHz) at the positions where the population reaches a minimum, and it reaches a maximum (29 kHz) at positions where the population is at a secondary maximum, according to Fig. 3. The experimental and theoretical values are roughly consistent except that the damped oscillation is not observed at z_2.

We thereby design an optimal flight parabola for atoms under two conditions: (1) each of three Raman pulses interacts with atoms with higher Raman transition efficiency; (2) the time interval T of the Raman pulses is as long as possible. The Raman beam that propagates downward is red-detuned by 2.08 MHz, while the Raman beam that propagates upward is blue-detuned by the same amount. Consequently, the atoms are launched at a velocity of 2.3 m/s, and the apex of their parabolic trajectory is at a position 12.7 cm inside the interference zones. The Raman π pulse is applied 10 ms before the apex, and T is 120 ms, corresponding to the positions where the Raman pulse interacts with the atoms successively at 4.2, 12.6, and 6.7 cm inside the interference zones.

V. GRAVITY-GRADIENT MEASUREMENTS

We test the designed flight trajectory for atoms by observing the interference fringes. First, we choose a chirp rate of 25 MHz/s for the Raman laser to compensate for gravity, and the duration of the Raman π pulse is set as 20 μs. Once

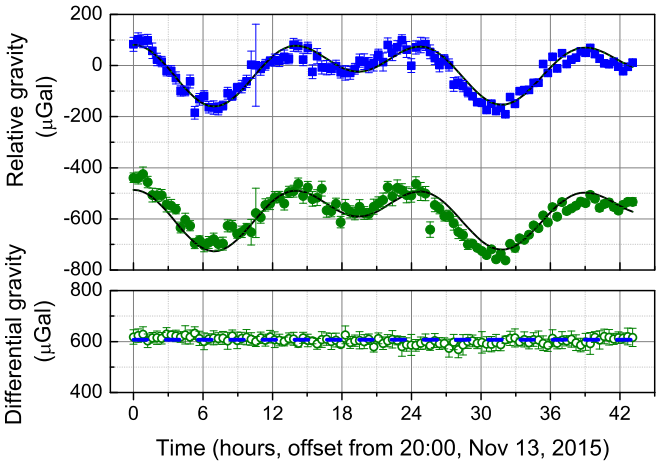

FIG. 5. Experimental data of the Earth's tides and differential gravity measured by the two AIs. The blue squares and the green dots are tidal signals monitored by interference zone 1 and interference zone 2, respectively. The black lines are calculations with tidal model. The green circles in the bottom panel are differential gravity measurements, and the blue dashed line is the fitted value.

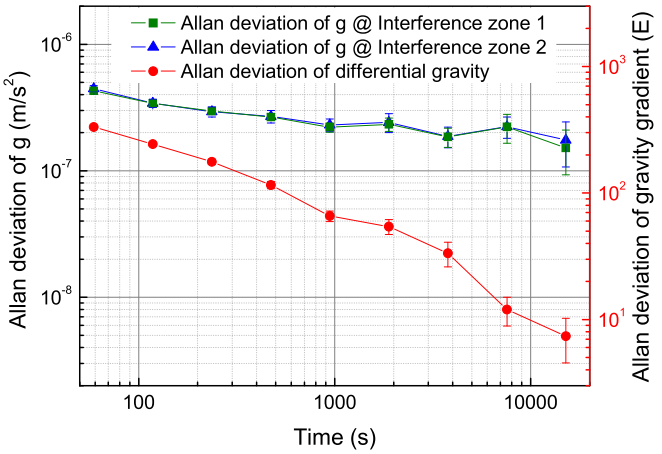

FIG. 6. Allan deviation of gravity and gravity-gradient measurements (1 E = 1×10^{-9} s^{-2}).

the atoms are launched to the interference zones, they are transferred from the $F = 3$, $m_F = 0$ to the $F = 2$, $m_F = 0$ state by a Raman π pulse, and then the atoms in the $F = 3$ state are blown away by a 1-ms pulse that is resonant with the $F = 3$ to $F' = 4$ transition. Subsequently, the Raman $\pi/2$-π-$\pi/2$ pulse sequence is applied to form atom interference loops, where the population in the $F = 3$ state is detected by a 5-ms pulse that is resonant with the $F = 3$ to $F' = 4$ transition, the phase of the second $\pi/2$ pulse is scanned by a step of $\pi/20$, and the atom interference fringes are obtained by recording the population versus phase. We obtain interference fringes with a signal-to-noise ratio (SNR) of 100:1, and the fringe contrasts for IZ1 and IZ2 are 24% and 18%, respectively. The differential gravity, Δg, is given by the phase difference between IZ1 and IZ2; the phase difference, $\Delta\phi$, is extracted by ellipse fitting [26]; and the gravity gradient is deduced from Δg and the baseline. In the ellipse fitting process, an ellipse is formed when the fringes from IZ1 are plotted versus those from IZ2, and the differential phase can be extracted from the ellipse fit parameters. Because the differential phase is too small to be exactly extracted by the ellipse fitting, we apply a pulsed magnetic field to the atoms in IZ2 to shift the differential phase by $\sim\pi/2$, whereupon the differential phase can be extracted by the ellipse fitting [27].

We estimate the ability of the gravity gradiometer to suppress the tidal effect by performing a 42-h-long measurement, which lasted from 20:00 of November 13 to 14:00 of November 15 in 2015, and from which the differential acceleration, Δg, can be obtained from the differential phase of the ellipses, $\Delta\phi$. The measurements are shown in Fig. 5, plotting the local gravitational acceleration values measured by IZ1 (blue squares in Fig. 5) and IZ2 (green dots in Fig. 5), and the calculations using a tidal model (black lines in Fig. 5). It can be seen that the temporal variation of the local gravity measured by the two AIs agrees with the tidal model. Both of the AIs have sensitivities that are almost equivalent, and the standard deviations are better than $2 \times 10^{-8} g$ over the 42 h. The measured Δg (green circles in Fig. 5) are scattered around the line where the tidal signal is canceled (blue dashed line in Fig. 5), and only the noncommon mode phase noise remains.

The performance of the gravity-gradient measurement is evaluated by the Allan deviation, for which the two AIs are continuously run for 24 h with a sample rate of 0.68 Hz, and 56 000 data points are obtained. Each 40-point ellipse is used to extract a differential phase by ellipse fitting, and 1400 differential phases are obtained and converted to gravity-gradient values by dividing by a scale factor of $k_{\text{eff}} T^2 L$, where, $k_{\text{eff}} = 1.6 \times 10^5$ cm^{-1} is the effective Raman wave vector, and L is the baseline. Meanwhile, both local gravity measurements are calculated by sine fitting from the individual fringes, and the Allan deviation is then calculated based on these measurements, as shown in Fig. 6. The values of the differential gravity are plotted (left y axis in Fig. 6) with those of the corresponding gravity gradient (right side y axis in Fig. 6).

Each data point in the Allan deviation curves (green squares for IZ1 and blue triangle blocks for IZ2 in Fig. 6) is obtained from a 40-point fringe. The resolutions of both AIs have the same Allan deviation curves and their resolutions reach 1.5×10^{-7} m/s^2, which is mainly limited by vibrational noise. The gravity gradient is not affected by the common-mode phase noise and consequently its Allan deviation(red dots in Fig. 6) sharply decreases. The resolution of the differential gravity measurement is 4.9×10^{-9} m/s^2 @ 15 000 s, and the corresponding resolution of the gravity-gradient measurement according to the 66.35-cm baseline is 7.4 E @ 15 000 s.

We also demonstrate a static measurement of the gravity gradient using the mass-modulation method. The local gravity gradient is modulated by a test mass of 824 kg that is composed of 73 lead bricks. These lead bricks are stacked compactly and placed on a homemade wheeled table, where the centroid position of the bricks is as high as the geometric center of the two AIs. This test mass is placed alternately at two fixed positions with a constant spacing. The measured shift of the gravity gradient is found to be (221 ± 56) E, which is extracted by subtracting the averaged gravity gradients at

the two positions. This measurement roughly agrees with the theoretical value of (251 ± 13) E.

VI. DISCUSSION

The resolution of the differential gravity acceleration reported herein is comparable to that of the dual-AI gravity gradiometers reported by McGuirk and co-workers [6,9] and Yu *et al.* [14]. Compared with the recent result of a single-AI gravity gradiometer reported by Sorrentino *et al.* [7], the advantage of our dual AI is the higher sampling rate, while there is still room for improvement in the resolution. The main limitations for the current resolution include a less-desirable SNR (100:1) and fringe contrast (18%–24%), amplitude noise, noncommon mode vibrational noise, and stray magnetic fields (1 μT). To improve the SNR and fringe contrast, atom clouds with more than 5×10^8 atoms and colder than 1 μK should be involved in the interferometers. A normalized detection is necessary for suppressing the amplitude noise. Also, the noncommon mode vibrational noise can be further suppressed by using a vibration isolation system, and a stray magnetic field less than 0.1 μT is possible by designing new shielding. In addition, the current sampling rate (0.68 Hz) is expected to increase to 2 Hz, which can further improve the sensitivity. With these improvements, a better short-term sensitivity is expected in the near future. For some applications in navigation, geodesy, environmental survey, and resource exploration, the short-term sensitivity of the state-of-the-art AGG can meet the practical needs; however, the environmental adaptability, reliability, and sampling rate are necessary to be further improved.

VII. CONCLUSION

We investigated the effect of the location-dependent Raman transition in gravity-gradient measurements with a dual AI, where the optimal location for the Raman transition was determined and then applied in gravity-gradient measurements. The gravity gradiometer was built based on a dual ^{85}Rb AI with a baseline of 66.35 cm. The saturated absorption spectra of ^{87}Rb atoms was used to control the detuning of the Raman beams for ^{85}Rb atoms. A gravity-gradient measurement using the differential AI with an optimized Raman transition was demonstrated, where the resolution of the gravity gradient is 7.4 E @ 15 000 s. The results are helpful for improving the design of compact and reliable gravity gradiometers. Further improvements will focus on improving the SNR, suppressing the noncommon mode vibration noise, and improving the magnetic field shielding.

ACKNOWLEDGMENTS

This work was supported by the National Key Research and Development Program of China under Grant No. 2016YFA0302002, and the National Natural Science Foundation of China under Grants No. 91536221, No. 11227803, and No. 11504411.

[1] L. Zhou, S. T. Long, B. Tang, X. Chen, F. Gao, W. C. Peng, W. T. Duan, J. Q. Zhong, Z. Y. Xiong, J. Wang, Y. Z. Zhang, and M. S. Zhan, Test of Equivalence Principle at 10^{-8} Level by a Dual-Species Double-Diffraction Raman Atom Interferometer, Phys. Rev. Lett. **115**, 013004 (2015).

[2] P. Berg, S. Abend, G. Tackmann, C. Schubert, E. Giese, W. P. Schleich, F. A. Narducci, W. Ertmer, and E. M. Rasel, Composite-Light-Pulse Technique for High-Precision Atom Interferometry, Phys. Rev. Lett. **114**, 063002 (2015).

[3] D. Durfee, Y. Shaham, and M. A. Kasevich, Long-Term Stability of an Area-Reversible Atom-Interferometer Sagnac Gyroscope, Phys. Rev. Lett. **97**, 240801 (2006).

[4] A. Peters, K. Y. Chung, and S. Chu, A measurement of gravitational acceleration by dropping atoms, Nature (London) **400**, 849 (1999).

[5] Z. K. Hu, B. L. Sun, X. C. Duan, M. K. Zhou, L. L. Chen, S. Zhan, Q. Z. Zhang, and J. Luo, Demonstration of an ultrahigh-sensitivity atom-interferometry absolute gravimeter, Phys. Rev. A **88**, 043610 (2013).

[6] J. M. McGuirk, G. T. Foster, J. B. Fixler, M. J. Snadden, and M. A. Kasevich, Sensitive absolute-gravity gradiometry using atom interferometry, Phys. Rev. A **65**, 033608 (2002).

[7] F. Sorrentino, Q. Bodart, L. Cacciapuoti, Y.-H. Lien, M. Prevedelli, G. Rosi, L. Salvi, and G. M. Tino, Sensitivity limits of a Raman atom interferometer as a gravity gradiometer, Phys. Rev. A **89**, 023607 (2014).

[8] X. C. Duan, M. K. Zhou, D. K. Mao, H. B. Yao, X. B. Deng, J. Luo, and Z. K. Hu, Operating an atom-interferometry-based gravity gradiometer by the dual-fringe-locking method, Phys. Rev. A **90**, 023617 (2014).

[9] J. B. Fixler, G. T. Foster, J. M. McGuirk, and M. A. Kasevich, Atom interferometer measurement of the Newtonian constant of gravity, Science **315**, 74 (2007).

[10] G. Lamporesi, A. Bertoldi, L. Cacciapuoti, M. Prevedelli, and G. M. Tino, Determination of the Newtonian Gravitational Constant Using Atom Interferometry, Phys. Rev. Lett. **100**, 050801 (2008).

[11] G. Rosi, F. Sorrentino, L. Cacciapuoti, M. Prevedelli, and G. M. Tino, Precision measurement of the Newtonian gravitational constant using cold atoms, Nature (London) **510**, 518 (2014).

[12] M. J. Snadden, J. M. McGuirk, P. Bouyer, K. G. Haritos, and M. A. Kasevich, Measurement of the Earth's Gravity Gradient with an Atom Interferometer-Based Gravity Gradiometer, Phys. Rev. Lett. **81**, 971 (1998).

[13] X. A. Wu, Gravity gradient survey with a moble atom interferometer, Ph.D. thesis, Stanford University, CA, 2009.

[14] N. Yu, J. M. Kohel, J. R. Kellogg, and L. Maleki, Development of an atom-interferometer gravity gradiometer for gravity measurement from space, Appl. Phys. B **84**, 647 (2006).

[15] M. Schmidt, M. Prevedelli, A. Giorgini, G. M. Tino, and A. Peters, A portable laser system for high-precision atom interferometry experiments, Appl. Phys. B **102**, 11 (2011).

[16] S. H. Yim, S. B. Lee, T. Y. Kwon, and S. E. Park, Optical phase locking of two extended-cavity diode lasers with ultra-low phase noise for atom interferometry, Appl. Phys. B **115**, 491 (2014).

[17] O. Carraz, F. Lienhart, R. Charrière, M. Cadoret, N. Zahzam, Y. Bidel, and A. Bresson, Compact and robust laser system for onboard atom interferometry, Appl. Phys. B **97**, 405 (2009).

[18] F. Theron, O. Carraz, G. Renon, N. Zahzam, Y. Bidel, M. Cadoret, and A. Bresson, Narrow linewidth single laser source system for onboard atom interferometry, Appl. Phys. B **118**, 1 (2015).

[19] J. K. Stockton, K. Takase, and M. A. Kasevich, Absolute Geodetic Rotation Measurement Using Atom Interferometry, Phys. Rev. Lett. **107**, 133001 (2011).

[20] K. Takase, Precision rotation rate measurements with a mobile atom interferometer, Ph.D. thesis, Stanford University, CA, 2008.

[21] M. Kasevich and S. Chu, Measurement of the gravitational acceleration of an atom with a light-pulse atom interferometer, Appl. Phys. B **54**, 321 (1992).

[22] O. Carraz, R. Charrière, M. Cadoret, N. Zahzam, Y. Bidel, and A. Bresson, Phase shift in an atom interferometer induced by the additional laser lines of a Raman laser generated by modulation, Phys. Rev. A **86**, 033605 (2012).

[23] G. W. Biedermann, X. Wu, L. Deslauriers, S. Roy, C. Mahadeswaraswamy, and M. A. Kasevich, Testing gravity with cold-atom interferometers, Phys. Rev. A **91**, 033629 (2015).

[24] M. Schmidt, A mobile high-precision gravimeter based on atom interferometry, Ph.D. thesis, Humboldt University, 2011.

[25] J. Ramirez-Serrano, N. Yu, J. M. Kohel, J. R. Kellogg, and L. Maleki, Multistage two-dimensional magneto-optical trap, Opt. Lett. **31**, 682 (2006).

[26] G. T. Foster, J. B. Fixler, J. M. McGuirk, and M. A. Kasevich, Method of phase extraction between coupled atom interferometers using ellipse-specific fitting, Opt. Lett. **27**, 951 (2002).

[27] Y. P. Wang, J. Q. Zhong, X. Chen, R. B. Li, D. W. Li, L. Zhu, H. W. Song, J. Wang, and M. S. Zhan, Extracting the differential phase in dual atom interferometers by modulating magnetic fields, Opt. Commun. **375**, 34 (2016).